Rapport de Stage

Contributions to the measurement of the $b\bar{b}$ cross section with ATLAS data at $\sqrt{s} = 7$ TeV

réalisé au

Centre de Physique des Particules de Marseille

et présenté à l'

Ecole Normale Supérieure de Lyon

S. K. Argyropoulos

Directeur: S.G. Muanza

Lyon 2010

S.K.A.

CONTENTS

ABSTRACT

Two original contributions to the measurement of the cross section for inclusive $b\bar{b}$ production at the ATLAS experiment are presented in this thesis. In the first part we calculate the inclusive cross section for bottom production at $\sqrt{s} = 7$ TeV at Next-to-Leading Order and including Next-to-Leading-Log resummation using the FONLL public code. In the second part, we present Jet Energy Scale Corrections originally derived for $\sqrt{s} = 14$ TeV and establish their validity for $\sqrt{s} = 7$ TeV by reconstructing the invariant mass of a $b\bar{b}$ pair coming from the decay of a Higgs boson with $m_H = 120$ GeV. The study is carried out on a Monte Carlo sample.

CHAPTER 1

MOTIVATION

Jets originating from b-quarks, also known as b-jets, play a key role in the ATLAS physics program. Looking at the Standard Model cross section for pp collisions (Fig 1.1), one can directly observe that b-quark production provides a major contribution to the total cross section. A correct identification of b-jets is thus crucial for the suppression of the light flavor QCD background and for the study of rare events involving b-jets. These include precision measurements of top quark properties, the search for the Higgs boson and also beyond Standard Model physics searches, notably the search for Supersymmetry. Given the very large branching ratio for the decay of a top quark into a bottom
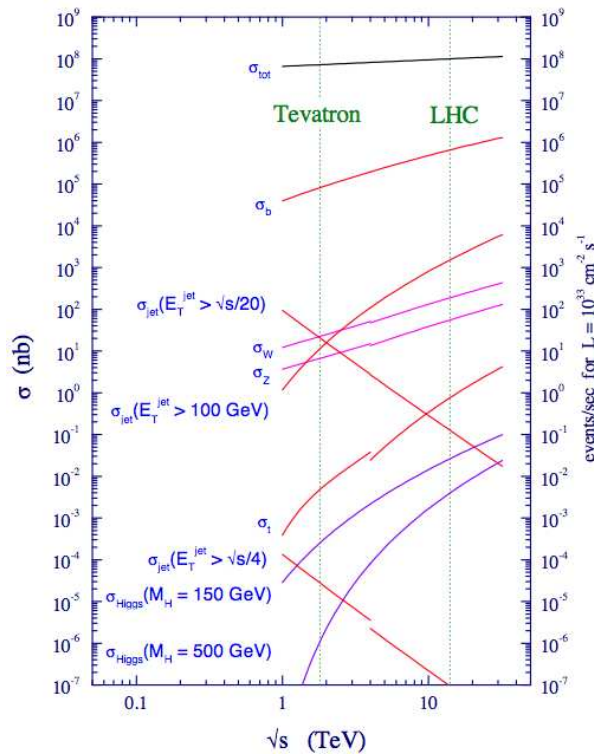
FIGURE 1.1: Predicted contributions to the Standard Model cross section for pp collisions. Figure extracted from [1].

quark[1], b-jets are present in practically every top decay event and are thus indispensable for the identification of top production events. We note for instance that the identification of the "golden

---

[1] Most recent measurements give $\left.\frac{\Gamma(Wb)}{\Gamma(Wq)}\right|_{q=b,s,d} = 0.99^{+0.09}_{-0.08}$ [2].

channel" of top production $t\bar{t} \to Wb\bar{W}\bar{b} \to (l\nu)b(jj)\bar{b}$ requires the successful tagging of one or two b-jets. An efficient b-tagging is thus necessary for reducing the signal-to-background ratio in top physics processes [3].

In the light Higgs hypothesis, which is favored by observations to date, the dominant decay mode is $H \to b\bar{b}$ (see Figure 1.2). Thus b-jet identication is also important for Higgs searches. Bottom quarks also appear in a number of decay channels of supersymmetric particles. The superpartners of the third generation of quarks are often the lightest quark superpartners and thus among the easiest to detect. For instance sbottom quarks are expected to decay to bottom quarks and neutralinos $\tilde{b} \to b + \tilde{\chi}_1^0$. Also, the gluino production of sbottom quarks via $pp \to \tilde{g}\tilde{g} \to \tilde{b}\bar{\tilde{b}}\tilde{b}\bar{\tilde{b}} \to (b\tilde{\chi}_0^1)\bar{b}(\bar{b}\tilde{\chi}_1^0)b$ has a distinctive signature involving 4 b-jets and large $\not{E}_T$ in the final state.
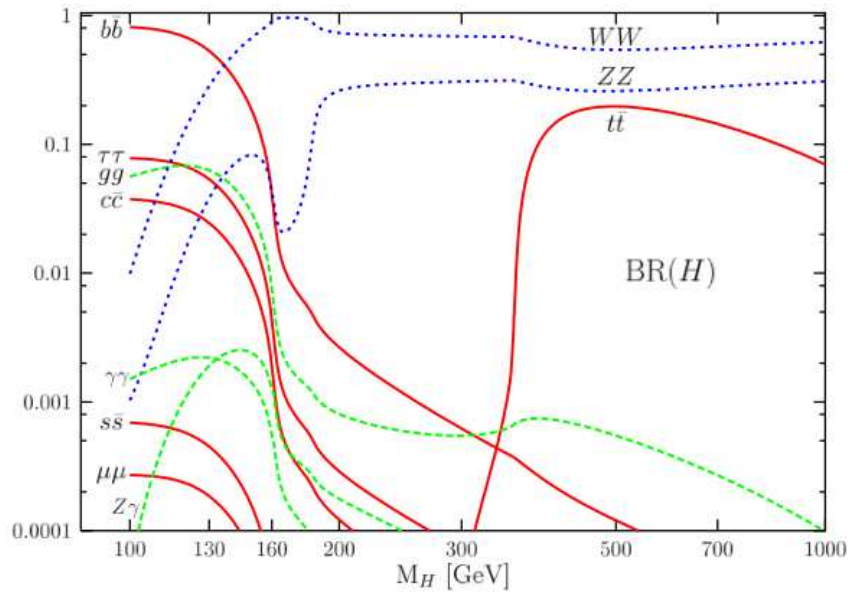
FIGURE 1.2: Standard Model Higgs branching ratios as a function of the Higgs mass. Figure extracted from [4].

It is evident from the above that the identification and study of b-jets is an essential ingredient for all major physics searches in the ATLAS collaboration. With the present work we aim at contributing (a) to ongoing work [5] for the calibration of b-tagging efficiencies in data with the System-8 and p_T^{rel} methods and (b) to the more precise determination of b-jet specific corrections, which are necessary for the study of processes described above.

CHAPTER 2

THE ATLAS EXPERIMENT

In this chapter we will give a brief description of the ATLAS experiment. For a more complete description we refer the reader to the original Technical Design Reports [6, 7] and the more recent [8].
The Large Hadron Collider is a proton-proton collider with a capability of reaching a center of mass energy $\sqrt{s} = 14$ TeV (i.e. 7 TeV per beam) and a luminosity of $L = 10^{34}$ cm^{-2}s^{-1}. After two startup periods with LHC working at $\sqrt{s} = 900$ GeV and later at $\sqrt{s} = 2.36$ TeV, from the beginning of 2010 the LHC has been operating at $\sqrt{s} = 7$ TeV and will continue collecting data delivering an expected 1 fb^{-1} of data until the end of 2011. After a 1 year shutdown the LHC is scheduled to restart operating at $\sqrt{s} = 14$ TeV in the beginning of 2013.
At design luminosity there will be 23 interactions per beam-crossing (most of them comprising minimum-bias events) giving a total of 40 million interactions per second (beam crossings being 25 ns apart). The guiding principle in the construction of the ATLAS experiment was the maximization of the discovery potential for new physics, notably the search for the Higgs boson and supersymmetry[1]. The study of such kind of events requires (a) a hermetic coverage in pseudorapidity and azimuthal angle for the accurate determination of $\not{E}_T$ and jet energy directions, (b) very good electromagnetic and hadronic calorimeters for precision measurements of EM and hadronic objects and (c) muon spectrometers with a capacity for high-precision muon measurements.
The overall detector layout is shown in Fig. A.1. The detector is composed of 4 major parts: (i) the inner detector, (ii) the calorimeter system, (iii) the muon spectrometers and (iv) the magnets.
The Inner Detector (depicted in Fig. A.2) measuring 7 m in length and 2.3 m in diameter is comprised of 3 subdetectors: (a) the pixel detector, (b) the Semiconductor Tracker (SCT) and (c) the Transition Radiation Tracker (TRT). It is immersed in a solenoidal magnetic field with intensity $B = 2$ T and has a pseudorapidity coverage of $|\eta| < 2.5$. With the use of very high-granularity detectors close to the interaction point the Inner Detector is used for the determination of impact parameters, particle momentum, vertexing and pattern recognition. The innermost layer of the Pixel Detector (called *B-layer*) is specially designed for identifying short-lived particles, such as B hadrons.
The calorimeter system (shown in Fig. A.3) is comprised of 3 parts: (a) the Electromagnetic calorimeter, (b) the Hadronic calorimeter and (c) the Forward calorimeters. Electromagnetic and Hadronic calorimeters are divided into two regions: (i) barrel, covering the pseudorapidity range and $|\eta| \leq 1.475$ (EMCal) and $|\eta| \leq 1.7$ (HCal) and (ii) End Cap, covering the pseudorapidity range $1.375 \leq |\eta| \leq 3$. (EMCal) and $1.5 \leq |\eta| \leq 3.2$ (HCal). The Electromagnetic (barrel and end-cap), Forward and Hadronic End Cap Calorimeters use Liquid Argon for the active medium and lead (EMCal), copper (HCal and FCal) or tungsten (FCal) for the absorbers. The Hadronic barrel Calorimeter uses plastic scintillating tiles embedded in an iron absorber. The calorimeter system measures the energy and momentum of electromagnetic and hadronic objects, providing a very good jet and $\not{E}_T$ performance, which is necessary for the study of many physics channels.

---

[1]Such events are expected to be extremely rare. For instance the rate of production of a light standard model Higgs boson is expected to be of the order of 1 per 10 billion events(see Fig. 1.1).

The calorimeter system is surrounded by a toroidal magnet system and the muon spectrometer. The strong magnetic field produced by the toroidal magnets minimizes the probability of multiple scatterings. The muon spectrometer consists of muon chambers utilizing different detector technologies to measure muons. The barrel chambers are arranged concentrically to the beam axis covering the pseudorapidity range $|\eta| < 1$ while the end cap chambers are arrange in four disks disks transverse to the beam axis, covering the range $1 < |\eta| < 2.7$.

Conventions

In the ATLAS experiment the coordinate systems in use are defined as follows. The beam direction defines the z-axis and the $x - y$ plane is the plane transverse to the beam direction. The positive x-axis points from the interaction point towards the center of the LHC ring and the positive y-axis points upwards. The azimuthal angle ϕ is measured around the beam axis and the polar angle θ is measured from the beam axis. One most frequently uses the pseudorapidity variable, defined as $\eta = -\ln(\tan\theta/2)$. Transverse variables are defined in terms of their x and y components, e.g. for the transverse momentum we have $p_T = \sqrt{p_x^2 + p_y^2}$. One can also define a distance measure in (η, ϕ) space as $\Delta R = \sqrt{(\Delta\eta)^2 + (\Delta\phi)^2}$.

CHAPTER 3

THEORETICAL PREDICTIONS

In this chapter we will detail the calculation of the inclusive $b\bar{b}$ cross section (a) at the parton level and (b) at the jet level. The calculation will be done at Next-to-Leading Order (NLO) (i.e. $\mathcal{O}\left(\alpha_s^3\right)$) including the resummation of large logarithms with Next-to-Leading-Logarithmic (NLL) accuracy using the FONLL public code developped by M. Cacciari *et al* [9].

3.1 Parton level prediction

In recent years there have been considerable efforts in the determination of the p_T distribution for heavy quark production in hadron colliders (LEP, DESY, Tevatron). The large discrepancy[1] between data and NLO QCD predictions has stirred up a lot of theoretical undertaking that led to the development of the powerful resummation procedures described below.

At LO, heavy flavour production proceeds either through quark-antiquark annihilation or through gluon-gluon fusion, the latter being the dominant channel for proton-proton collisions at the LHC. However at NLO new production channels (e.g. gluon splitting and flavor excitation) appear, accounting for large contributions to the LO cross section. Since the cross section for $gg \rightarrow gg$ is about a hundred times bigger than the one for $gg \rightarrow Q\bar{Q}$, NLO corrections can be as large as the LO value[2], and thus NLO accuracy is necessary for a consistent treatment of heavy flavor production processes. Such processes (where $m_Q \gg \Lambda_{QCD}$) have a particular theoretical appeal due to the smallness of the coupling constant, which allows for a perturbative expansion of the differential cross section in powers of α_S[3]. However, at high collision energies, where $p_T \gg m_Q \gg \Lambda_{QCD}$, one can no longer choose a single characteristic scale between p_T and m. It has been proven [10] that in this 2-scale regime large logarithms $\mathcal{O}\left(\ln^m \frac{p_T}{m_Q}\right)$ appear in the perturbative expansion. These logarithms spoil the convergence of the perturbative expansion and have thus to be resummed to all orders. These

---

[1]Data for the total cross section for inclusive b production showed an excess by a factor of ~ 3 over NLO calculations. See [11] and references therein.

[2]At LO heavy quark production proceeds either through quark-antiquark annihilation $q\bar{q} \rightarrow Q\bar{Q}$ or gluon-gluon fusion $gg \rightarrow gg$. At NLO a gluon can split into a quark-antiquark pair with a probability $\sim \alpha_s$, giving rise to the process $gg \rightarrow gQ\bar{Q}$. See e.g. [10].

[3]We remind that at NLO the running coupling is given by

$$\alpha_S(m_Q^2) = \frac{1}{b\ln\left(m_Q^2/\Lambda_{QCD}^2\right)}\left[1 - \frac{b'}{b}\frac{\ln\ln\left(m_Q^2/\Lambda_{QCD}^2\right)}{\ln\left(m_Q^2/\Lambda_{QCD}^2\right)}\right], \quad \text{with} \quad b = \frac{33 - 2N_f}{12\pi}, \; b' = \frac{153 - 19N_f}{24\pi^2}, \quad (3.1)$$

where N_f is the number of flavors.

terms can be classified as Leading Logarithmic (LL), Next-to-Leading Logarithmic (NLL) and so on:

$$\text{LL} \quad : \quad \alpha_S^2 \left(\alpha_S \ln \frac{p_T}{m_Q} \right)^k$$

$$\text{NLL} \quad : \quad \alpha_S^3 \left(\alpha_S \ln \frac{p_T}{m_Q} \right)^k \quad , \quad k \in \mathbb{N} \tag{3.2}$$

They stem from singularities appearing during the emission of collinear and soft gluons (which, at lower energies, are screened by m_Q). These kind of divergences can be systematically absorbed via the factorization theorem in the definition of non-perturbative parton distribution functions (or fragmentation functions) which in turn acquire a scale dependence. The differential cross section for the inclusive production of a hadron H_3 takes the form

$$\frac{d\hat{\sigma}_{H_1 H_2 \to H_3 X}}{dp_T}(s, m^2) = \frac{d\hat{\sigma}_{ij \to QX}}{dp_T} \left(xs, \mu_F \right) \otimes D^{QH_3}(xs, \mu_F), \tag{3.3}$$

where $\hat{\sigma}_{ij \to QX}$ is the partonic cross section, directly calculable in perturbative QCD. The dependence on the arbitrary scale μ_F[4] is a mere parametrization of large distance physics which cannot be described by perturbative QCD. It is obvious that observables like $\sigma_{H_1 H_2 \to H_3 X}$ cannot depend on such arbitrary scales, so to all orders of perturbation theory these scale dependencies must cancel out. However, when we truncate the perturbative expansion at some particular order, this cancellation will not be complete and thus cross sections will display a scale dependence.

The FONLL code provides for the calculation of the double differential cross section $\frac{d^2\sigma}{dp_T^2 dy}$ in hadron-hadron and photon-hadron collisions matching a Fixed Order calculation (at NLO accuracy) with NLL resummation. In the light of the above discussion, one can see the advantages of such an approach[5]:

- NLO calculation takes into account large corrections coming from $\mathcal{O}(\alpha_s^3)$ processes (eg gluon splitting, flavor excitation)

- resummation of large logarithms enables a better description at large p_T

- NLL accuracy lessens the scale dependence and will thus lead to narrower uncertainty bands for the cross section prediction

After integrating over rapidities, the FONLL output is schematically given by [9]

$$
\begin{aligned}
\frac{d\sigma}{dp_T^2} &= A(m)\alpha_s^2 + B(m)\alpha_s^3 \\
&+ \left[\alpha_s^2 \sum_{i=2}^{\infty} a_i \left(\alpha_s \ln \frac{\mu}{m} \right)^i + \alpha_s^3 \sum_{i=1}^{\infty} b_i \left(\alpha_s \ln \frac{\mu}{m} \right)^i \right] \times G(m, p_t) \\
&+ \mathcal{O}\left(\alpha_s^4 \left(\alpha_s \ln \frac{\mu}{m} \right)^i \right) + \mathcal{O}\left(\alpha_s^4 \times \text{PST} \right),
\end{aligned}
\tag{3.4}
$$

where PST stands for terms suppressed by powers of m/p_T in the large p_T limit and G is an arbitrary function subject to the constraint $G(m, p_T) \to 1$ as $m/p_T \to 1$[6]. The FONLL code is based on the

---

[4]We note that $\hat{\sigma}$ also depends on the renormalization scale through the running coupling $\alpha_s = \alpha_s(\mu_R)$. This dependence reflects another type of singularity (UV) stemming from the exchange of virtual gluons. Here we have suppressed the μ_R dependence for simplicity.

[5]We must also note that in the FONLL implementation the non-perturbative b fragmentation functions measured at LEP were re-extracted and properly matched to the perturbative calculation fixing the historical discrepancy between heavy flavour cross section measurements and theoretical calculations.

[6]Here we will present only the key ingredients that are relevant to the calculation, directing the avid reader to the original publications [9, 11].

choice of G made in [9], i.e.

$$G(m, p_T) = \frac{p_T^2}{p_T^2 + 25m^2}. \tag{3.5}$$

The FONLL code requires the following input from the user: the energy and type of colliding beams, the Parton Distribution Function sets, the value of the heavy quark mass, the value of factorization and renormalization scales, and lastly the values of p_T and rapidity y. The uncertainty of the cross section has 3 major contributions coming from: PDF uncertainty, mass uncertainty and scale uncertainty.

In our study we use the FONLL built-in PDF library with the PDF set CTEQ6.1M [12]. The PDF's are constructed by minimizing a chi-square function

$$\chi'^{\,2} = \sum_e \chi_e^2(a, r), \tag{3.6}$$

where e denotes the experimental datasets, a are the n PDF parameters ($n = 20$ for CTEQ6.1M) and r a set of Gaussian random variables. The global minimum with respect to a and r represents the best fit to the data. The corresponding uncertainties are calculated with the aid of the Hessian matrix

$$H_{ij} \equiv \frac{1}{2} \frac{\partial^2 \chi'^2(a, \hat{r}(a))}{\partial a_i \partial a_j}. \tag{3.7}$$

More precisely, one defines n directions corresponding to the eigenvectors of the Hessian matrix and calculates the excursions from the global minimum χ_0' in the "+" and "−" direction along the eigenvectors. One obtains in this way $2n$ PDF sets which parametrize the area of the global minimum (central PDF). The PDF-related uncertainties are then calculated by the master formulae [1]:

$$\Delta X_{\max}^+ = \sqrt{\sum_{i=1}^{20} \left[\max\left(X_i^+ - X_0, X_i^- - X_0, 0\right)\right]^2}, \tag{3.8}$$

$$\Delta X_{\max}^- = \sqrt{\sum_{i=1}^{20} \left[\max\left(X_0 - X_i^+, X_0 - X_i^-, 0\right)\right]^2}. \tag{3.9}$$

As far as the choice of mass is concerned, we take the value of the mass used in the CTEQ6.1M fit, that is $m_b = 4.5$ GeV, keeping the relative errors calculated in the $\overline{\text{MS}}$-scheme for consistency [2][7]:

$$m_b = 4.5^{+0.18(4.05\%)}_{-0.08(1.67\%)} \text{ GeV}. \tag{3.10}$$

Finally for the QCD scales we choose $\mu_R = \mu_F = \mu_0$, where μ_0 is calculated dynamically according to the formula $\mu_0 = m_T = \sqrt{m_b^2 + p_T^2(b)}$[8]. The corresponding error is obtained by varying μ_0 over the range $[\mu_0/2, 2\mu_0]$. Scanning over y bins $[0, \pm 0.5, \pm 1.0, \pm 1.5, \pm 2.0, \pm 2.5, \pm 3.0]$ and p_T bins $[0.1, 0.25, 0.5, 0.75, 1, 2.5, 5, 7.5, 10, 25, 50, 75, 100, 250, 500, 750, 1000]$GeV and integrating over the rapidities, we obtain the p_T distribution shown in Figure 3.1. Integrating over p_T we get the total cross section for inclusive b production

$$\sigma(0.1 \leq p_T \leq 1000 \text{ GeV}) = 266 \; ^{+29(10.9\%)}_{-29(10.9\%)_{PDF}} \; ^{+13(4.9\%)}_{-26(9.8\%)_{m_b}} \; ^{+3(1.1\%)}_{-10(3.8\%)_{QCD}} \; \mu\text{b}. \tag{3.11}$$

The total uncertainty curve in Figure 3.1 is then obtained by summing the individual uncertainty contributions in quadrature

$$\delta \left.\frac{d\sigma}{dp_T}\right|_{tot} = \sqrt{\left(\delta \left.\frac{d\sigma}{dp_T}\right|_{PDF}\right)^2 + \left(\delta \left.\frac{d\sigma}{dp_T}\right|_m\right)^2 + \left(\delta \left.\frac{d\sigma}{dp_T}\right|_{QCD}\right)^2}. \tag{3.12}$$

---

[7]Consistency requires that the central value and uncertainty on the b-quark mass be defined in the same renormalization scheme as the one used in the input PDF set.

[8]This choice slightly underestimates the uncertainties related to the variation of QCD scales. See [11].
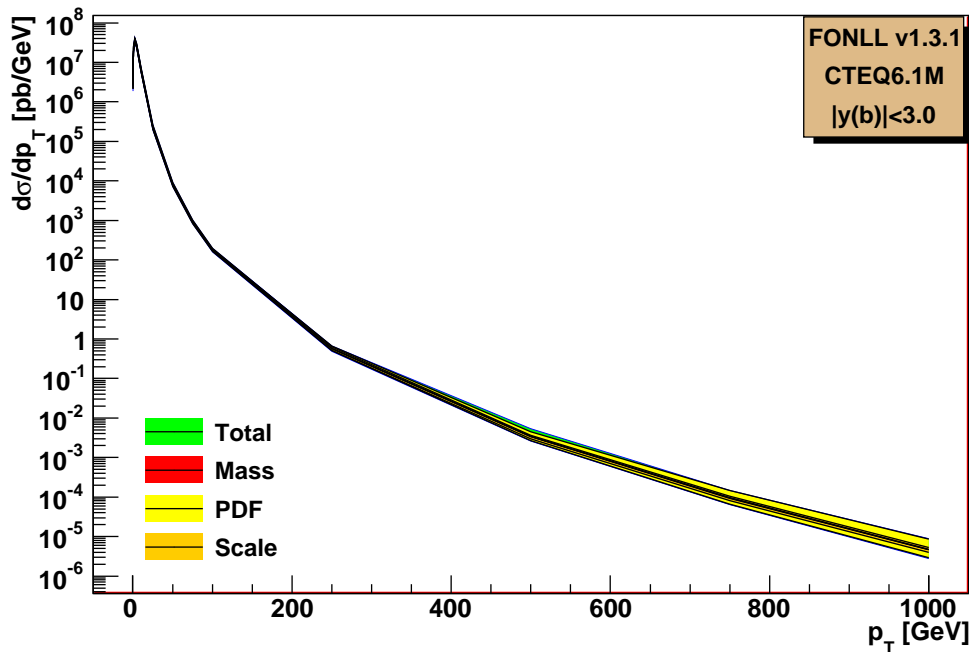
FIGURE 3.1: p_T distribution for inclusive b-quark production in pp collisions at $\sqrt{s} = 7$ TeV. Colored bands represent uncertainties related to the choice of PDF's, scale and heavy quark mass.

Integrating $\frac{d\sigma}{dp_T} + \delta \left.\frac{d\sigma}{dp_T}\right|_{tot}$ and $\sigma - \delta \left.\frac{d\sigma}{dp_T}\right|_{tot}$ over the whole p_T spectrum, we obtain

$$\sigma(0.1 \leq p_T \leq 1000 \text{ GeV}) = 266 \,^{+39(14.7\%)}_{-45(16.9\%)} \,\mu\text{b} \tag{3.13}$$

The same calculation at Fixed Order (no resummation) yields a central value of $\sigma(0.1 \leq p_T \leq 1000 \text{ GeV}) = 252 \,\mu$b. We see thus that the NLL resummation provides a marginal enhancement by 5.6% over the Fixed Order result. However the NLL result differs significantly from the Fixed Order result, especially in the high-p_T region. More precisely the NLL resummation leads to narrower uncertainty bands and thus to a better description of the p_T distribution compared to the Fixed Order result[9]. By inspecting the uncertainty contributions to the p_T distribution, one can see that in the regions $0 \lesssim p_T \lesssim 7$ GeV and $300 \lesssim p_T \lesssim 1000$ GeV the PDF related uncertainty dominates, while in the intermediate region $7 \lesssim p_T \lesssim 300$ GeV the uncertainty is mainly due to the choice of scale. This behaviour is to be expected, since at very low and very high p_T PDF's (especially those related to gluon distribution) are not known with good accuracy [1].

3.2   Jet level prediction

The FONLL code provides us with the cross section for inclusive b-quark production. However, what we need for this study is the cross section for inclusive b-jet production. To pass from the parton level to the level of particle jets we need to fragment all partons. This can be done with event generators like PYTHIA, which contain hadronization models and parton showers. A potential problem arises here since event generators containing the necessary fragmentation models use LO matrix elements[10].

---

[9]See the discussion at the beginning of this Section and also [9].

[10]For MC@NLO there is no official ATLAS production of $b\bar{b}$ samples at $\sqrt{s} = 7$ TeV. We also note that parton shower algorithms in PYTHIA include a resummation of soft and collinear logarithms at LL accuracy.

To remedy this, we reweight the p_T distribution obtained from PYTHIA (LO) with the p_T distribution obtained by FONLL (NLO+NLL) using an overall normalization factor

$$R = \frac{\sigma_{\text{parton,FONLL}}}{\sigma_{\text{parton,PYTHIA}}} \tag{3.14}$$

and transferring the shape of the p_T distribution via the function

$$C(p_T) = \frac{\left.\frac{d\sigma}{dp_T}\right|_{\text{parton,FONLL}}}{\left.\frac{d\sigma}{dp_T}\right|_{\text{parton,PYTHIA}}}. \tag{3.15}$$

For the latter we need a continuous function matching our FONLL result, so we fit the FONLL p_T distribution using an overconstrained fit given by the following function

$$
\begin{aligned}
\left.\frac{d\sigma}{dp_T}\right|_{\text{parton,FONLL}} &= e^{16.9347} e^{0.929545 \ln p_T} e^{-0.192167(\ln p_T)^2} e^{-0.199752(\ln p_T)^3} e^{-2.35026\cdot 10^{-2}(\ln p_T)^4} \\
&\times e^{1.13181\cdot 10^{-2}(\ln p_T)^5} e^{-2.90086\cdot 10^{-4}(\ln p_T)^6} e^{-2.18993\cdot 10^{-4}(\ln p_T)^7} e^{1.57143\cdot 10^{-5}(\ln p_T)^8}
\end{aligned} \tag{3.16}
$$

The fitted function together with the uncertainty envelope (fit to total uncertainty bands) is given in Figures 3.2 and 3.3. Opting for an overconstrained fit ensures that the errors resulting from the fitting procedure are negligible compared to the uncertainty in the theoretical calculation. In the

FIGURE 3.2: Fits to theoretical prediction for the p_T distribution in inclusive b-quark production at $\sqrt{s} = 7$ TeV in the range $0 \leq p_T \leq 1000$ GeV.

same way, one should then find a function describing the p_T distribution for inclusive b production obtained by PYTHIA. The latter can be established from a Monte Carlo $b\bar{b}$ sample by plotting the number of b quarks as a function of the p_T of the leading b quark. Normalizing the FONLL and
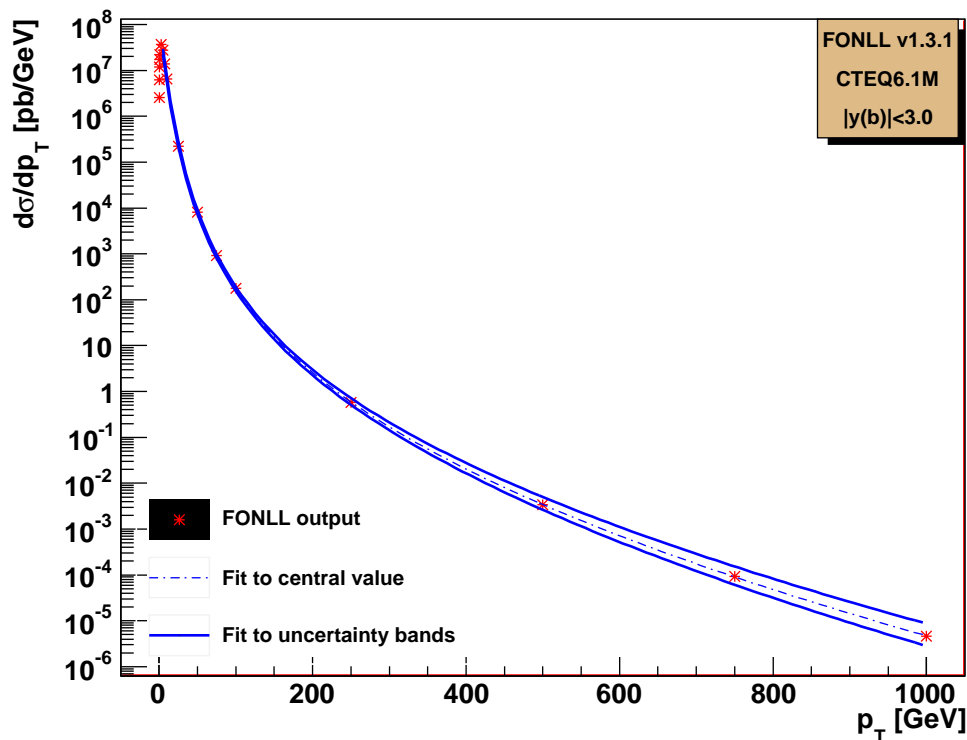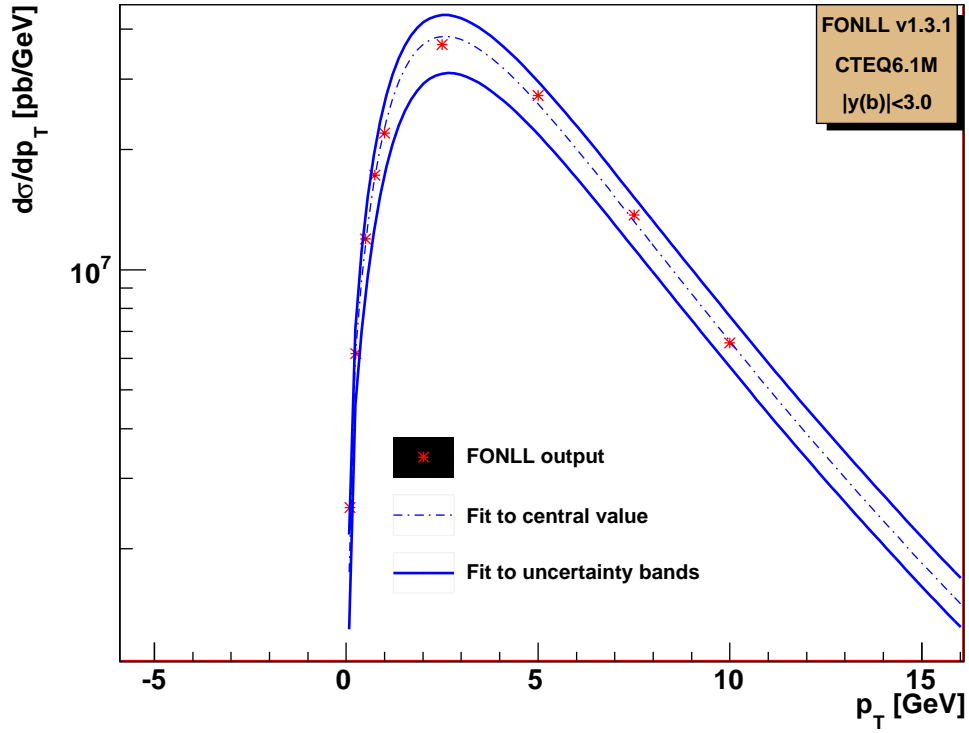
FIGURE 3.3: Fits to theoretical prediction for the p_T distribution in inclusive b-quark production at $\sqrt{s} = 7$ TeV in the range $0 \leq p_T \leq 16$ GeV.

PYTHIA distributions to unity (i.e. setting $R = 1$), one can obtain the p_T distribution for inclusive b-jet production at NLO+NLL order by

$$\frac{d\sigma}{dp_T}\bigg|_{bjet,NLO+NLL} = C(p_T) \left.\frac{d\sigma}{dp_T}\right|_{bjet,PYTHIA}. \tag{3.17}$$

We note that $\frac{d\sigma}{dp_T}\big|_{bjet,PYTHIA}$ is obtained from a Monte Carlo $b\bar{b}$ sample by plotting the number of b-jets as a function of the p_T of the leading b-jet.

Chapter 4

MEASUREMENT OF THE $b\bar{b}$ CROSS SECTION

4.1 Jet Reconstruction Algorithms

Although the theoretical construction of the theory of strong interactions is based on $SU(3)_c$ gauge symmetry, it is well known that no physical observable displays signs of such a symmetry (*color confinement*). Quarks and gluons produced in hadron collisions fragment and hadronize, producing collections of colorless collimated hadrons called *jets*. In order to study jet properties in an experiment, one needs a set of rules for grouping particles into jets. Over the years several jet algorithms have been constructed and there is no universal jet algorithm for all topologies, since different classes of algorithms are better suited to the study of specific topologies than others. For an overview and comparison of different jet algorithms we refer the reader to [13]. Here we will only describe the general characteristics of jet reconstruction algorithms and focus on the *anti-k_t* algorithm, which is the default used in ATLAS analyses.

Jet reconstruction algorithms need to satisfy a minimum set of properties adopted by the Snowmass Accord [14]. These demand that a jet algorithm: be simple in implementation, be defined at any order in perturbation theory, yield finite cross sections at any order in perturbation theory and be insensitive to hadronization. A jet reconstruction algorithm must also be associated with a recombination scheme, which indicates what momentum to assign to the combination of two particles. With time it became clear that jet properties defined by the Snowmass accord were incomplete and one needed a more stringent jet definition. The general guidelines for jet reconstruction in ATLAS were extracted from [15]. The major theoretical guidelines are **infrared** and **collinear safety**, i.e. the number and kinematics of jets remains the same after adding an infinitesimally soft parton or replacing a parton by two collinear partons and **order independence**, i.e. the same hard scattering should be reconstructed independently at parton, particle and detector level. Major experimental guidelines include **detector technology independence**, **environment independence** (independence of pileup, underlying activity etc) and **implementation**.

The anti-k_T algorithm [16] belongs to the class of sequential recombination algorithms. Pairs of input objects i, j are analyzed by defining the distance measures

$$
\begin{aligned}
d_{iB} &= k_{t_i}^{2p} \\
d_{ij} &= \min(k_{t_i}^{2p} m k_{t_j}^{2p})\frac{\Delta R_{ij}^2}{R^2}
\end{aligned}
\tag{4.1}
$$

where d_{ij}, d_{iB} the distance between 2 entities (particles or pseudojets) or an entity and the beam respectively, R the radius parameter[1], p a parameter governing the relative power of the energy versus geometrical (Δ_{ij}) scales ($p = -1, +1$ for the anti-k_T,k_T algorithms respectively) and $\Delta R_{ij}^2 = (y_i - y_j)^2 + (\phi_i - \phi_j)^2$, with y and ϕ the rapidity and azimuth of said entities. The anti-k_t algorithm

---

[1]In this study we choose $R = 0.4$.

is Infrared and Collinear safe.

The process described above refers to *particle jets*. On an experimental level one also uses *calorimeter jets* which are objects defined in terms of calorimeter cells. Signals coming from individual cells are combined into larger signal objects: *calorimeter towers* and *topological cell clusters*. The former constitute a collection of calorimeter cells with a fixed $\Delta\eta \times \Delta\phi$. The latter are formed by an iterative procedure, starting with a seed cell which passes a certain significance threshold[2] and incorporating in the cluster all neighboring cells until one reaches the region of cells with $\Gamma = 0$ (no energy is deposited in the cell). For the purpose of jet-finding, towers and clusters are treated as massless pesudoparticles and assigned a four-momentum calculated from the reconstructed energy according to the following prescription

$$
\begin{aligned}
E = p &= \sqrt{p_x^2 + p_y^2 + p_z^2} \\
p_x &= p\frac{\cos\phi}{\cosh\eta} \\
p_y &= p\frac{\sin\phi}{\cosh\eta} \\
p_z &= p\tanh\eta.
\end{aligned}
\tag{4.2}
$$

4.2 b-tagging

b-tagging is the identification of jets containing a b-quark. A high b-tagging efficiency is of vital importance for the study of physics processes that involve b-quarks[3], since these suffer from very large backgrounds coming from light-flavored jets. To define b-tagging performance one uses the Monte Carlo event history to find the flavor of the parton from which the jet originated. More precisely, if a b quark with $p_T > 5$ GeV is found in the Monte Carlo truth record within a cone of radius $\Delta R = 0.3$ around the jet direction, the jet is labelled as a true b-jet. To quantify b-tagging performance one uses the following variables: the *tagging efficiency*, defined as the fraction of true b-jets tagged as b-jets over the total number of taggable[4] b-jets and the *mis-tagging* rate, defined as the fraction of true b-jets that are not b-tagged over the total number of taggable b-jets. The performance of a b-tagging algorithm is usually given as a function of tagging efficiency versus *jet rejection*, which is defined as the inverse of the mis-tagging rate.

The identification of b-jets relies on the properties of b-quarks which distinguish them from light quarks. For instance, B-hadrons retain a large fraction of the original b quark momentum and their decay products can have a large p_T with respect to the jet axis (p_T^{rel}), due to the high mass of the b quark. Most importantly, B-hadrons are relatively long-lived, which means that a B-meson produced at the primary vertex will travel a distance $\langle l \rangle = \beta\gamma c\tau \sim$ mm before decaying, thus producing a displaced secondary vertex (on the contrary light-flavored hadrons are short lived and decay in the primary vertex). One can distinguish thus three main categories of tagging algorithms used in ATLAS: impact parameter taggers, secondary vertex taggers and soft lepton taggers.

Impact parameter tagging algorithms measure the impact parameter (i.e. the point of closest approach) of tracks with respect to the primary vertex. Supposing that (x_0, y_0) is the point of closest approach to the point of interaction $(0,0)$, one can define a *transverse impact parameter* on the (x, y) plane as

$$
d_0 = -x_0 \sin\phi + y_0 \cos\phi.
\tag{4.3}
$$

---

[2]The significance Γ is defined as the signal-to-noise ratio, i.e. $\Gamma = E_{cell}/\sigma_{noise,cell}$.

[3]See Chapter 1.

[4]A jet is considered as *taggable* if it passes the cuts $p_T > 15$ GeV and $|\eta| < 2.5$.

In the same way one defines a *longitudinal impact parameter* on the plane (R, z) by

$$d_z = (z_V - z_0) \sin \theta, \tag{4.4}$$

where z_V is the z coordinate of the primary vertex, and z_0 is the z coordinate of the trace at the point of closest approach. A large d_0 allows the identification of particles coming from the decay of a B-hadron. If one further defines

$$\text{sign}(d_0) = \left(\vec{P}_j \times \vec{P}_t \right) \cdot \left[\vec{P}_t \times \left(\vec{X}_{PV} - \vec{X}_t \right) \right], \tag{4.5}$$

where $\vec{P}_j, \vec{P}_t$ are respectively the jet and track directions measured by the calorimeters and $\vec{X}_t, \vec{X}_{PV}$ are the positions of the tracks and primary vertex respectively, it turns out that tracks coming from heavy flavored hadrons tend to have a positive sign while the sign of tracks from light flavored hadrons is random [8]. In the same way one defines a sign for the longitudinal impact parameter by

$$\text{sign}(d_z) = (\eta_j - \eta_t) z_{0t}. \tag{4.6}$$

Thus one can define 3 impact parameter taggers: IP1D relying on d_z, IP2D relying on d_0 and IP3D combining the previous two.

Secondary vertex taggers are based on the explicit (inclusive or exclusive) reconstruction of the secondary interaction vertex, pertaining to the decay of B-hadrons. To reconstruct an inclusive secondary vertex, one starts with building two-track pairs that form a vertex with $\frac{L_{3D}}{\sigma_{L_{3D}}} > 2$ and $L_{3D} \equiv ||\vec{X}_{PV} - \vec{X}_t||$. All remaining tracks are combined in an inclusive vertex iteratively until the χ^2 of the fit is good. One studies the following properties of secondary vertices: the invariant mass of tracks associated to the vertex, the ratio of the sum of the energies of the tracks participating to the vertex to the sum of the energies of all tracks in the jet and the number of two-track vertices. The SV1 algorithm uses a 2D-distribution of the two first variables and a 1D-distribution of the number of two-track vertices, while the SV2 algorithm is based on a 3D-histogram of the three properties. The JetFitter algorithm uses information on the topological structure of weak decays of beauty and charmed hadrons.

Lastly soft lepton taggers rely on the identification of leptons coming from leptonic decays of heavy flavored hadrons inside the jet. The procedure relies on the reconstruction of soft leptons and their matching to heavy-flavored jets. Soft leptons are reconstructed by a combination of 2 algorithms. A combined muon for instance corresponds to a track fully reconstructed in the muon spectrometer which is matched to a track in the inner detector. The applied cuts for combined muons are $p_T > 3$ GeV, $|d_0| < 4$ mm and $\Delta R < 0.5$, where $\Delta R = \sqrt{(\Delta \eta)^2 + (\Delta \phi)^2}$ is the distance from the jet axis. After soft lepton reconstruction and matching, a likelihood ratio is used to distinguish heavy-flavored from light-flavored jets[5]. This technique is limited by the leptonic branching ratios of heavy quarks but exhibits a very high purity and low correlations with track-based algorithms making it ideal for cross-calibration.

4.3 Energy Scales

The determination of the kinematics of the particles produced in a collision event is of prime importance for physics analyses. Particle kinematics is determined by the tracking system (trajectories), the calorimeter system (energy) and muon spectrometers. Here we will focus on the calorimeter system and hence the determination of the energy of different objects.

In an experiment one measures two main classes of objects: electromagnetic objects (photons, charged

---

[5]For details see [8] and references therein.

leptons) and QCD objects (hadons and jets). An experimental measurement consists of electronic signals coming from different parts of the detector. In order to compare the experimental measurement with the theoretical calculations, one must then convert these electronic signals to physical quantities (here, the amount of energy deposited in the calorimeters). This calibration produces a distinct energy scale for each class of objects. We thus refer to objects measured in the *electromagnetic* (EM) scale and the *hadronic* and *jet energy scales*.

EM Scale

The determination of the EM scale consists mainly in reducing the ECAL output signals to the energy deposited in the calorimeter cells. This can be done by studying either single particles or well-documented resonances such as $Z \rightarrow e^- e^+$[6]. In the latter case the calibration can be done by imposing the constraint that the invariant mass of the decay products be the same as the measured resonance mass.

The energy deposited by a particle in the EM calorimeter is given by

$$
\begin{aligned}
E_{cal} &= C_{cal}(X,\eta)\left(1 + f_{out}(X,\eta)\right)E_{cl}, \\
X &= \frac{\sum_{i=1}^{3} E_i X_i + E_{ps} X_{ps}}{\sum_{i=1}^{3} E_i + E_{ps}}.
\end{aligned}
\tag{4.7}
$$

where E_{cl} is the energy deposited in a given cluster (only in the ionization medium), X is the longitudinal barycenter of shower depth expressed in radiation lengths computed from the centre of the detector, η is the cluster barycenter, f_{out} is the fraction of the energy deposited outside the cluster and C_{cal} is the calibration factor defined as the ratio between the true energy deposited in the calorimeter (absorbers and ionization medium) and the reconstructed energy E_{cl}.

The corrections are derived by Monte Carlo and tested with test beams (e ,μ ,π for the electomagnetic calorimeter or stable hadrons for the calibration of the hadronic calorimeter). The calibration factor derived by test beam data is in excellent agreement with Monte Carlo results.

Jet Energy Scale

The precise definition of the Jet Energy Scale (JES) is important for numerous physics measurements, such as the determination of the top mass m_t, the reconstruction of jet resonances, the measurement of inclusive jet cross sections and the quality of missing transverse energy measurements which is of paramount importance for new physics searches at the LHC.

The ultimate goal of JES corrections is the reconstruction of the initial parton energy from calorimeter jets. This procedure is divided into two steps: (a) correcting calorimeter jets to particle jets and (b) correcting particle jets to initial partons[7]. In the first step, one has to account for all detector-specific effects, such as calorimeter non-compensation, electronics noise, losses due to cracks and dead material, etc. In the second step one corrects for physics effects, such as initial and final state radiation, clustering, hadronization effects, pileup, flavor dependency of JES corrections etc.

The basic idea behind JES corrections is to assume a known EM scale and use events containing a well-measured EM object balanced by jets to determine the jet response. This involves a number of sub-corrections which are applied in a sequential manner, as described by the formula:

$$
E_{jet}^{corr} = \frac{E_{jet}^{meas} - O}{F_\eta \cdot R \cdot S} k_{bias}.
\tag{4.8}
$$

---

[6]The process $Z \rightarrow e^- e^+$ is a prime example of a benchmark process: it has very low background, the Z mass has been measured with a good accuracy and its decay products leave big energy deposits in the ECAL. See [17] for more details.

[7]In many cases JES is established on the particle level and one does not attempt to trace this procedure back to the parton level.

The first step, called *offset correction* (O), is to subtract the energy not associated to the hard scatter (i.e. underlying event, noise, multiple interactions and signal pileup). The *absolute jet response* R is given by

$$R = 1 + \frac{\not{E}_T \cdot \vec{p}_T^{\,\gamma}}{\left(\vec{p}_T^{\,\gamma}\right)^2}, \tag{4.9}$$

where $\not{E}_T$ is the missing transverse energy and $\vec{p}_T^{\,\gamma}$ is the momentum of the photon measured in back-to-back γ+jets events. The *relative response correction F_η* (or η-intercalibration) accounts for non-uniformities in the response as a function of pseudorapidity. The *showering correction S* corrects for energy leakage outside (inside) the jet cone from particles inside (outside) the jet cone. This parameter depends on the jet reconstruction algorithm and for the k_T-class of algorithms $S = 1$. Lastly, k_{bias} represents any additional biases, such as minimum bias events that pass the zero suppression threshold or biases related to the determination of the absolute response correction.

In the ATLAS implementation of JES corrections one does not take into account the offset correction. The rest of the correction factors have been derived by Monte Carlo studies and are parametrized by the formula

$$R_{jet} = \left[1 + a_1(\eta)(\ln p_T)^{-1} + a_2(\eta)(\ln p_T)^{-2} + a_3(\eta)(\ln p_T)^{-3} + a_4(\eta)(\ln p_T)^{-4}\right]^{-1}. \tag{4.10}$$

The corrected energy and transverse momentum of the jet are then given by

$$
\begin{aligned}
E_{corr} &= \sqrt{\frac{p_T^2(R^2 - 1) + E^2(1 - \tanh^2 \eta)}{1 - \tanh^2 \eta}}, \\
p_{Tcorr} &= R p_T.
\end{aligned}
\tag{4.11}
$$

Muonic Jet Energy Scale

A significant improvement on the jet energy scale can be achieved by identifying jets which contain neutrinos. More precisely, since neutrinos cannot be detected, they introduce a systematic underestimation of the p_T of the jet, which is estimated to be of the order of 10% [18]. Here we will restrict our attention to the study of muonic decays of b-jets.

At the parton level, a b-quark almost always decays to a c quark, which in turn decays into an s or a d quark. The W bosons produced in the process can decay either hadronically to $q\bar{q}$ or leptonically to $l^+\nu_l$ (cascade decay) or $l^-\bar{\nu}_l$ (direct decay). Bottom jets are consequently classified into 3 categories according to their decay modes: (i) *hadronic*, if both W's decay hadronically, (ii) *semileptonic*, if only one of the W's decays into leptons and (iii) *leptonic*, if both W's decay leptonically. Taking into account the hadronic and leptonic branching ratios of the W bosons, which are respectively $B(q\bar{q}) = 2/3$ and $B(l\nu) = 1/3$, we find that the probability that a b-jet decay semileptonically is $P_{semileptonic} = 4/9 \approx 44.44\%$ and for a fully leptonic decay $P_{leptonic} = 1/9 \approx 11.11\%$. If we further demand that the lepton be of a specific flavor (e.g. muon[8]) the respective probabilities become $P_{semimuonic} = 12/81 \approx 14.8\%$ and $P_{muonic} = 1/81 \approx 1.2\%$. We immediately observe that, in more than half of the cases, a b-jet will contain at least one neutrino and given the non-negligible p_T fraction carried by the neutrino, we conclude that neglecting leptonic corrections can lead to a significant degradation of the jet energy scale.

Since muons are most easily identifiable among leptons, a first step towards a better determination of the jet energy is the muonic jet energy scale (JESMU). The basic idea behind JESMU involves tagging b-jets that contain muons and correcting the jet energy scale through a parametrization of the energy carried away by the neutrino. JESMU corrections are entirely based on Monte Carlo studies and the

---

[8]Here, the term *semimuonic* is used with an exclusive meaning, i.e. it designates jets containing exactly one muon and no other leptons. Later the term semimuonic will be used with an inclusive meaning.

procedure is detailed below.

The JESMU corrections are established using b-jets from a $t\bar{t}$ sample. Performance is studied on $t\bar{t}$ samples as well as $b\bar{b}$ samples constructed from dijet samples. Lastly the impact of JESMU corrections can be studied by reconstructing the invariant mass of $b\bar{b}$ pairs coming from the decay of Higgs bosons. The official ATLAS JESMU corrections were derived for $\sqrt{s} = 14$ TeV using the following setup [18]. Muons were reconstructed with the Staco algorithm[9] [19], jet reconstruction was based on a topocluster seeded cone algorithm [20] and b-tagging was based on a soft muon tagger[10]. A b-jet is considered semileptonic if a muon neutrino coming from a B or D-hadron is found in the decay chain of the original b-quark.

The energy of the neutrino can be calculated from Monte Carlo and parametrized in terms of b-jet and muon kinematics. The contribution of the neutrino transverse momentum to the total p_T of the jet depends on its angle with respect to the jet axis. This angle is not strongly correlated with muon and jet kinematics, so it cannot be estimated accurately. The neutrino energy doesn't provide any angular information, so it can neither be used to parametrize the fraction of energy carried away by the neutrino. To integrate angular correlations one uses the response function

$$R_{semileptonic} = \frac{p_{T,\text{reco}}^{\text{jet}+\mu}}{p_{T,\text{True}}^{\text{jet}+\mu+\nu}}, \tag{4.12}$$

where $p_{T,\text{reco}}^{\text{jet}+\mu}$ is the perpendicular component of the vector addition of the reconstructed jet and reconstructed muon and $p_{T,\text{True}}^{\text{jet}+\mu+\nu}$ is the perpendicular component of the vector addition of the true jet, true muon and true neutrino momenta. The corrected p_T is then given by

$$\vec{p}_T^{\,corr} = C\vec{p}_{T\text{reco}}^{\,\text{jet}+\mu}, \tag{4.13}$$

with

$$C = \langle R_{semileptonic} \rangle^{-1} \tag{4.14}$$

calculated in different $p_{T,\text{reco}}^{\mu}/p_{T,\text{reco}}^{\text{jet}}$ bins to integrate the angular correlations between neutrino and jet-muon kinematics and $\langle R_{semileptonic} \rangle$ representing the mean of the gaussian fit to the $R_{semileptonic}$ distribution.

4.4 Correction validation

In this section we will study the impact of the JES corrections described above in the reconstruction of the invariant mass of a $b\bar{b}$ pair coming from the decay of a Higgs boson with mass $m_H = 120$ GeV. The Monte Carlo samples used in this study are

```
mc09_7TeV.105872.WH120bb_pythia.merge.AOD.e521_s765_s767_r1302_r1306
```

```
mc09_7TeV.105872.WH120bb_pythia.merge.AOD.e521_s765_s767_r1250_r1260.
```

with a total statistics of 99980 events. Datasets have been reprocessed with the B-Tagging ntuple format. These samples contain events coming from the decay chain $q\bar{q} \to W \to WH \to (l\nu_l)(b\bar{b})$, where b quarks fragment and hadronize into b-jets and can further decay either (semi-)leptonically or hadronically. The invariant mass of the $b\bar{b}$ system is given by

$$m = \sqrt{(E_1 + E_2)^2 - (p_{x,1} + p_{x,2})^2 - (p_{y,1} + p_{y,2})^2 - (p_{z,1} + p_{z,2})^2} \tag{4.15}$$

---

[9]Staco muons are muons reconstructed in the muon spectrometer and matched in an inner detector track.

[10]See section 4.2 above. In [18], b-tagging required the existence of a b-quark in the Monte Carlo truth record within a radius $\Delta R < 0.3$ from the jet axis.

or in terms of available ntuple variables

$$
\begin{aligned}
m &= \big[(E_1 + E_2)^2 - (p_{T,1}\cos\phi_1 + p_{T,2}\cos\phi_2)^2 - (p_{T,1}\sin\phi_1 + p_{T,2}\sin\phi_2)^2 \\
&\quad - (E_1\tanh\eta_1 + E_2\tanh\eta_2)^2 \big]^{1/2},
\end{aligned} \tag{4.16}
$$

where indices $1,2$ refer to the leading and subleading b-jet and ϕ_i, η_i are the azimuth and pseudo-rapidity of the i-th b-jet with respect to the beam axis. Quantities in the ntuples are measured in the Electromagnetic Scale. To show the effect of JES and JESMU corrections, the invariant mass reconstruction is carried out in 3 steps

1. No corrections applied (EM scale)

2. Application of Jet Energy Scale corrections

3. Application of Muonic Jet Energy Scale corrections

The cleaning cuts applied to the sample are

- exactly 2 b-jets in event

- at least 1 reconstructed primary vertex

- at least 2 reconstructed tracks associated to leading and subleading b-jets

- $|\eta_1| < 2.5$ and $|\eta_2| < 2.5$

- $\Delta R_{b-jets} > 0.8$

where

$$
\begin{aligned}
\Delta R_{b-jets} &= \sqrt{(\Delta\eta_{b-jets})^2 + (\Delta\phi_{b-jets})^2} \\
\Delta\eta_{b-jets} &= |\eta_1 - \eta_2| \\
\Delta\phi_{b-jets} &= \min\left(|\phi_1 - \phi_2|, |2\pi - |\phi_1 - \phi_2||\right).
\end{aligned} \tag{4.17}
$$

The first cut is applied in order to eliminate b-jets originating from gluonic bremsstrahlung[11]. The cut in pseudorapidity ensures that the analyzed b-jets are within the η-coverage limits of the Inner Detector and Calorimeter regions where precision measurements can be performed. The last cut is applied in order to ensure that the analyzed b-jets are two distinct objects[12].

It was observed that the sample is contaminated with low-p_T light-flavored jets that contribute to low-energetic tails in the invariant mass spectrum. A percentage of b-jets with very low p_T can also contribute to these tails. Thus in order to obtain a symmetric peak, we are forced to introduce a further kinematic cut on the p_T of light-flavored and b-tagged jets

- $p_{T,1} > 10$ GeV and $p_{T,2} > 10$ GeV (EM scale)

- $p_{T,1} > 20$ GeV and $p_{T,2} > 20$ GeV and $p_{T,LF} > 10$ GeV (after JES and JESMU corrections)

---

[11]We note that b-jets coming from gluonic bremsstrahlung tend to have low-p_T, while the invariant mass reconstruction uses only the leading and subleading (high-p_t) b-jets.

[12]We remind that b-jets are reconstructed with a cone of radius $R = 0.4$. We have observed that there were some events containing b-jets with overlapping jet cones.

where $p_{T,i}, p_{T,LF}$ is the transverse momentum of the i-th b-jet and light-flavored jets respectively. For the study of muonic jet energy scale corrections, one needs to define different categories according to the decay modes of b-jets. In principle, given enough statistics, one could define these categories in an exclusive manner. However in this study and in the official ATLAS study study of JESMU corrections [18], all categories were defined in an inclusive manner, with respect to muons and muonic neutrinos found in the Monte Carlo truth record[13]. These are detailed in the following table.

Category	Definition
inclusive	all events that pass cleaning cuts are considered
had_had	no μ and no ν_μ in b-jets
had_1mu	exactly 1 μ or exactly 1 ν_μ in one b-jet and no μ and no ν_μ in remaining b-jet

Since the b-jets originate from an unstable resonance, we expect that the b-jet invariant mass follow a Breit-Wigner distribution. However, since we are studying reconstructed jets, i.e. jets after interaction with the detector, we expect the detector's response to affect the form of the invariant mass distribution. Since the detector's response is largely Gaussian, we choose to fit the invariant mass distribution with a (non-relativistic) Breit-Wigner distribution convoluted with a Gaussian, i.e. a Voigt distribution

$$V(x; \sigma, \Gamma) = \int_{-\infty}^{+\infty} \frac{e^{-(x-x')^2/2\sigma^2}}{\sigma\sqrt{2\pi}} \frac{\Gamma/2}{\pi(x'^2 + \Gamma^2/4)} dx', \tag{4.18}$$

where σ is the standard deviation of the Gaussian distribution and Γ is the decay width of the resonance (both distributions are centered at $x_0 = 0$). In what follows we will only concentrate on the determination of the expectation value and the standard deviation of the Voigtian distribution, which express the resonance mass and the energy resolution respectively. For this reason we hold the decay width fixed to its default PYTHIA value $\Gamma_H = 3.081$ MeV. The fit covers the Full Width at Half Maximum of the Voigt distribution. The fit results for each of the three steps described above are given in the tables below.

EM Scale fits

Category	HISTO		FIT			
	MPV	RMS	Peak	Γ	σ	χ^2/ndf
Inclusive	62.02	15.16	63.39 ± 0.11	3.081	14.57 ± 0.15	35.58/16
had_had	65	15.29	67.03 ± 0.13	3.081	12.84 ± 0.19	35.67/14
had_1mu	56.19	16.84	57.4 ± 0.2	3.081	16.57 ± 0.26	46.31/18

The presence of undetected neutrinos in semileptonic b-jets (had_1mu) causes (a) a shift of the invariant mass towards lower values and (b) a deterioration of the energy resolution, as expected.

JES correction fits

Category	HISTO		FIT			
	MPV	RMS	Peak	Γ	σ	χ^2/ndf
Inclusive	97.3	19.5	100.8 ± 0.2	3.081	17.1 ± 0.3	32.15/18
had_had	101.3	18.62	104.7 ± 0.2	3.081	14.74 ± 0.33	35.19/16
had_1mu	89.55	20.7	91.91 ± 0.42	3.081	20.5 ± 0.7	33.11/21

---

[13]We note that in [18] the definition of respective categories relied only on muonic neutrinos. Here for technical reasons we were forced to use muons in addition to muonic neutrinos so as to increase the statistics.

We observe that the application of JES corrections shifts the invariant mass peaks by a factor ~ 1.6. We notice however a deviation of the peak in the case of a completely hadronic decay (had_had) with respect to the expected value $m_H = 120$ GeV. This indicates that JES corrections give a satisfactory but not completely accurate estimate of the Jet Energy Scale. This however is to be expected, since JES corrections were derived solely from Monte Carlo studies, leaving ample room for improvement (cross-checking with data, possibly further refining corrections on a parton level).

Appendix A

THE ATLAS DETECTOR
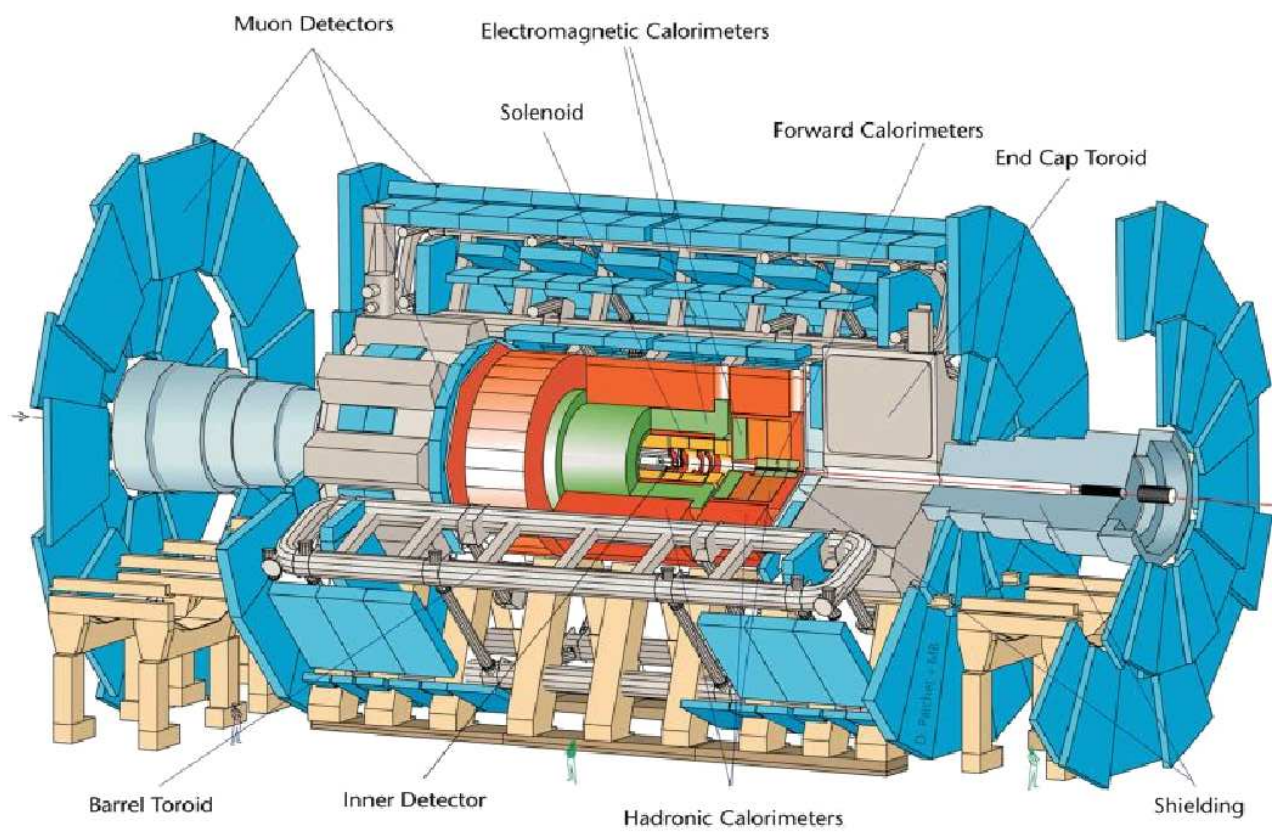
FIGURE A.1: Layout of the ATLAS detector.

6.2m

2.1m

Barrel semiconductor tracker

Pixel detectors

Barrel transition radiation tracker

End-cap transition radiation tracker

End-cap semiconductor tracker
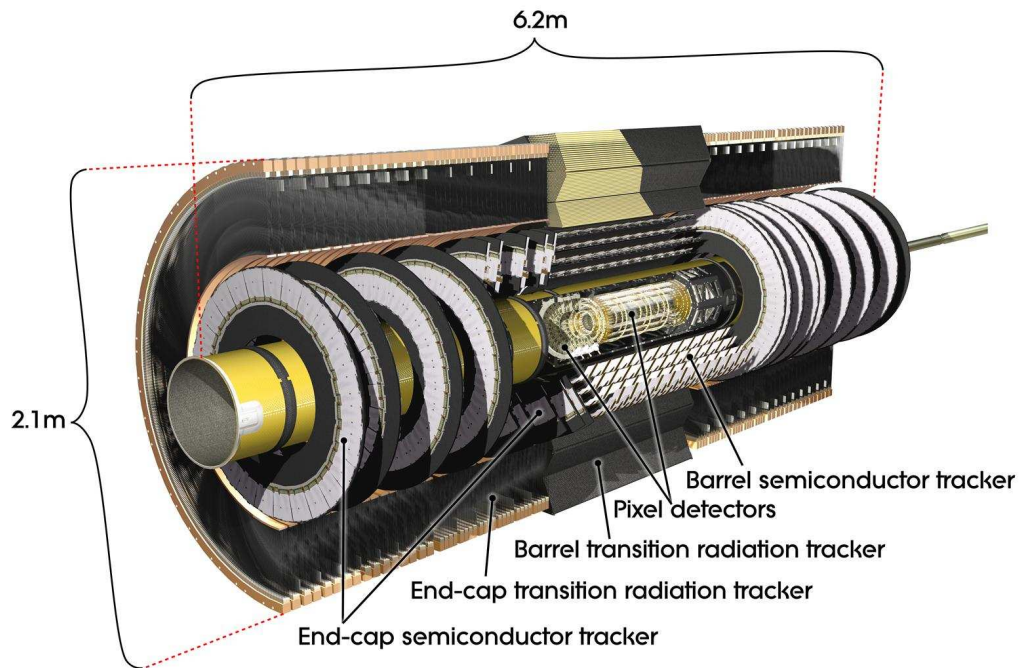
FIGURE A.2: Layout of the Inner Detector.

Tile barrel

Tile extended barrel

LAr hadronic
end-cap (HEC)

LAr electromagnetic
end-cap (EMEC)

LAr electromagnetic
barrel

LAr forward (FCal)
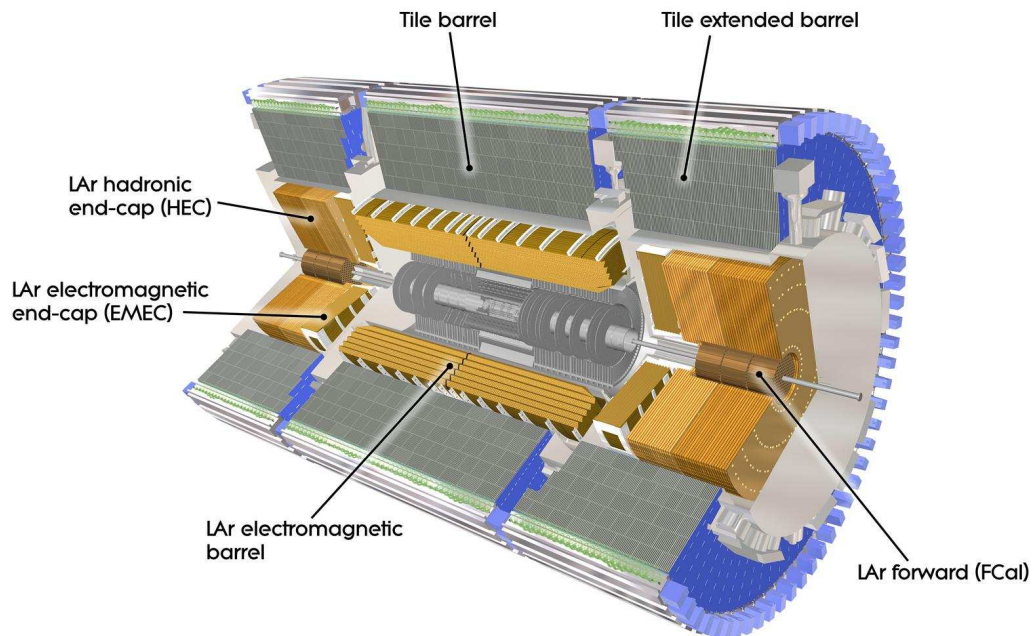
FIGURE A.3: Layout of the Calorimeter system.

APPENDIX B

JES CORRECTION VALIDATION FITS
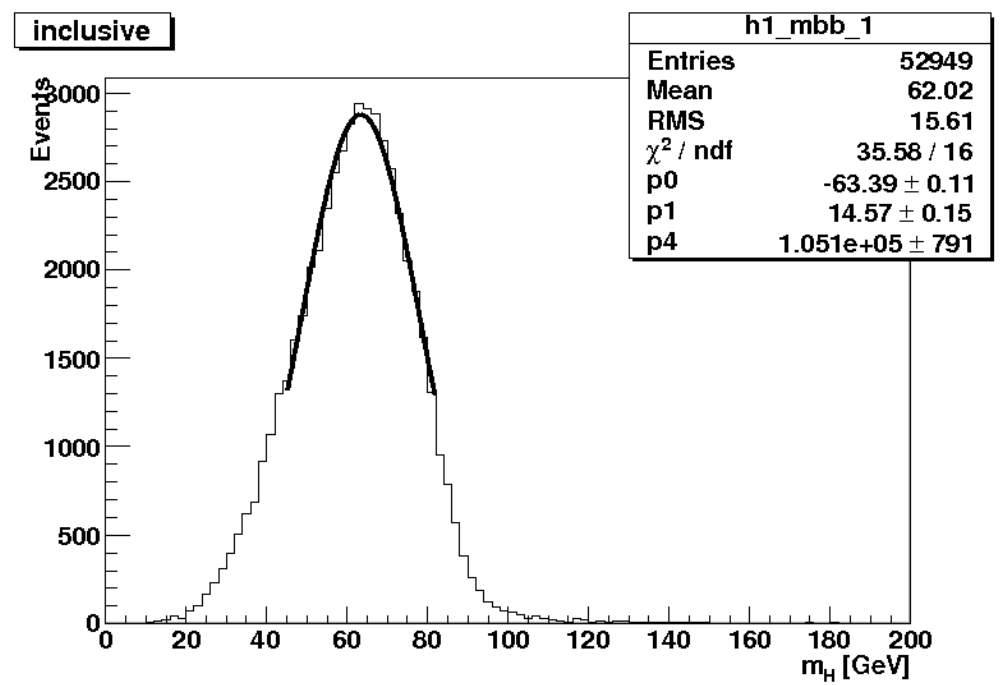
FIGURE B.1: EM Scale inclusive
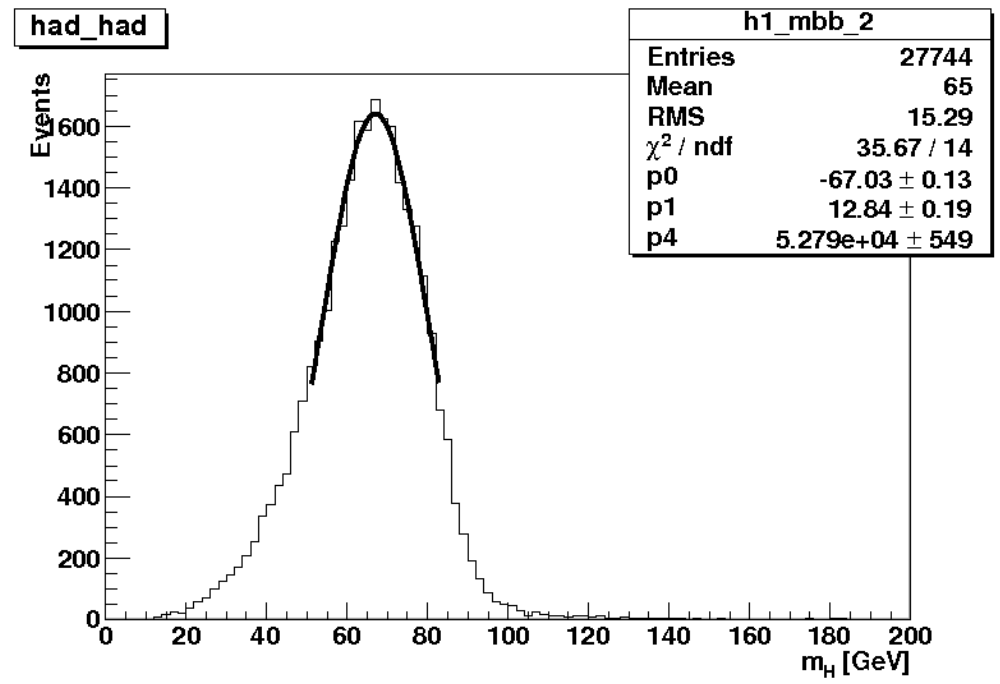
FIGURE B.2: EM Scale hadronic
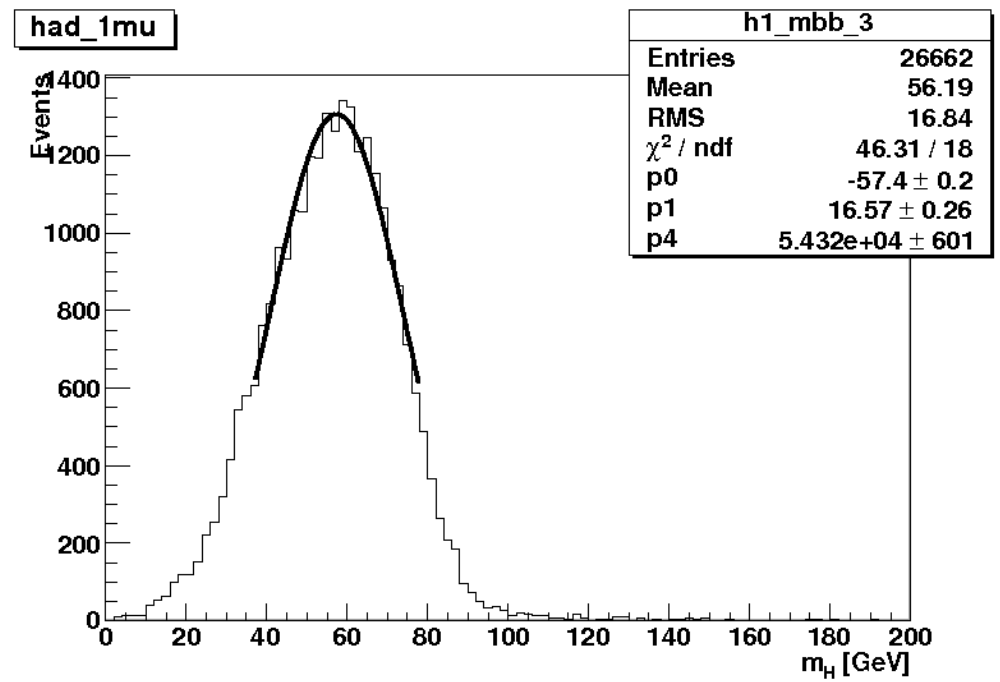
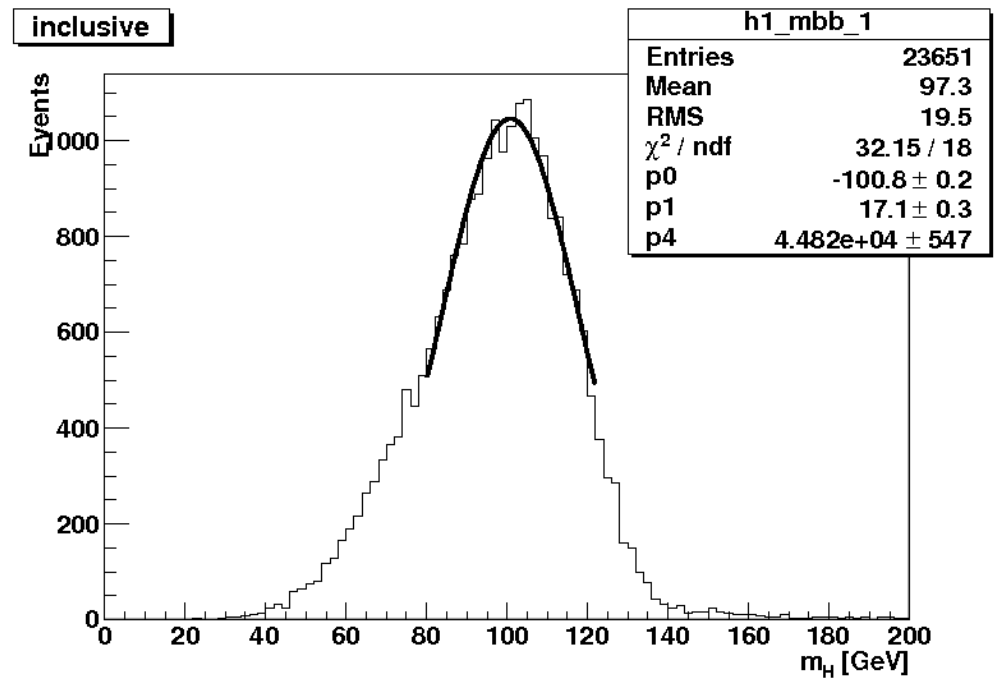

FIGURE B.3: EM Scale semimuonic
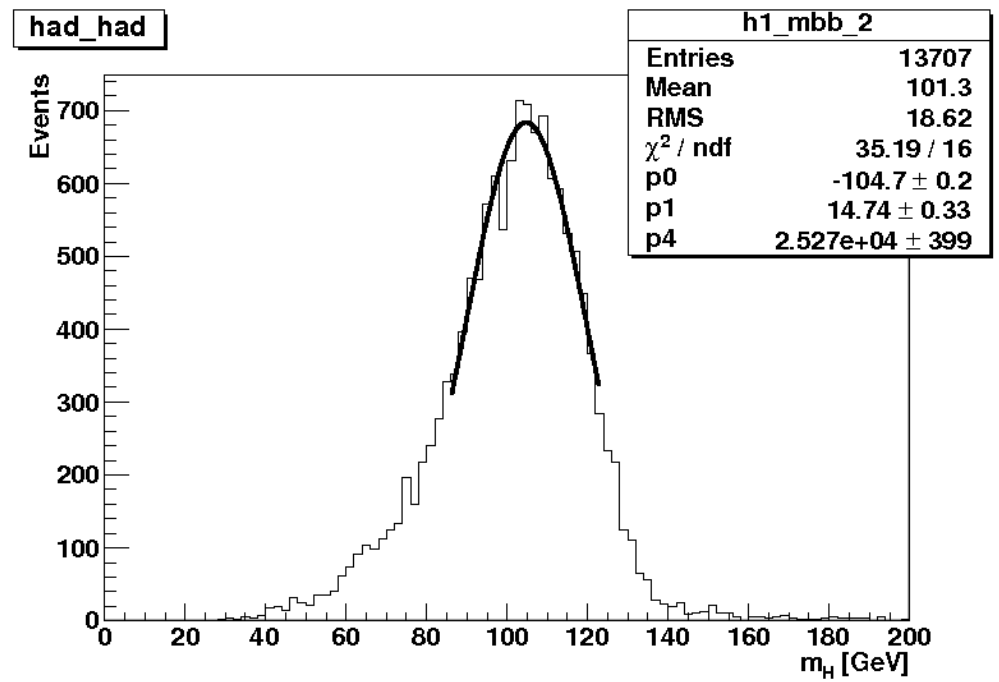
FIGURE B.4: JES inclusive

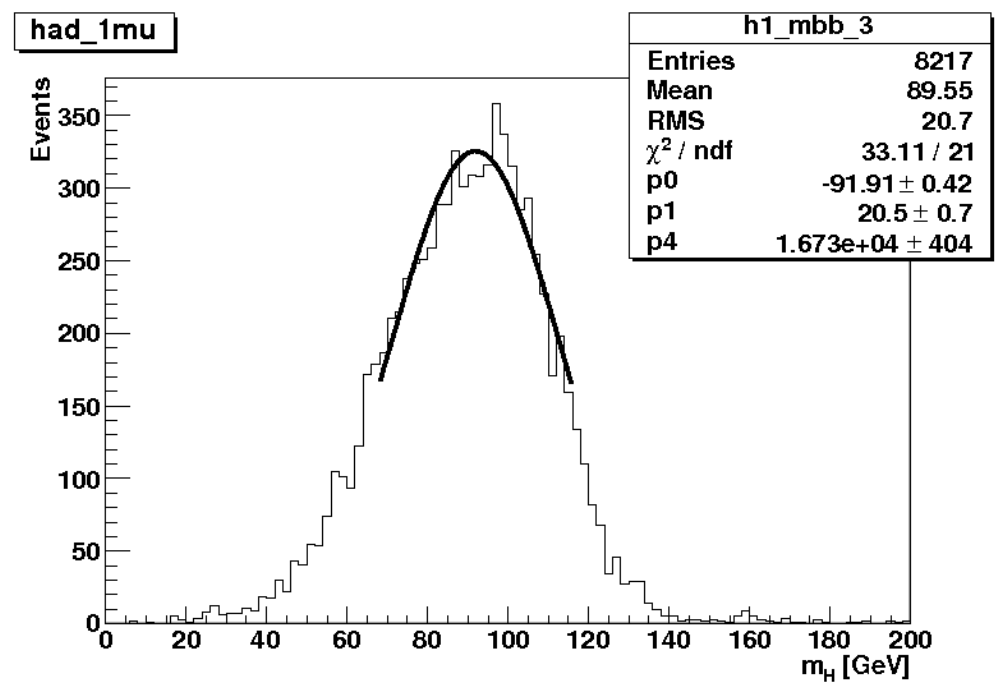**FIGURE B.5:** JES hadronic

FIGURE B.6: JES semimuonic

CONCLUSIONS AND PROSPECTS

We calculated the cross section for inclusive bottom production at NLO order both with and without NLL resummation at $\sqrt{s} = 7$ TeV using the FONLL public code. We found that NLL resummation provides an enhancement by 5.6% of the total cross section obtained at Fixed Order (no resummation) while reducing the uncertainty band at high-p_T. The result obtained was $\sigma(0.1 \leq p_T \leq 1000$ GeV$) = 266 \, ^{+39(14.7\%)}_{-45(16.9\%)}$ pb. We also showed that Jet Energy Scale corrections originally derived for $\sqrt{s} = 14$ TeV are also valid for $\sqrt{s} = 7$ TeV.

This work could be further extended and refined in various ways. As we showed, cross section uncertainties are mainly due to PDF-related uncertainties. Thus using a more recent PDF set from the LHAPDF library is expected to reduce the total cross section uncertainty. Following the procedure described in Section 3.2 one could also calculate the total cross section for inclusive b-jet production in a straightforward manner. Lastly, JESMU corrections originally derived for $\sqrt{s} = 14$ TeV remain to be validated for $\sqrt{s} = 7$ TeV using the procedure detailed in Section 4.4.

References

[1] J. M. Campbell, J. W. Huston, W. J. Stirling, *Rept. Prog. Phys.* **70** (2007) 89 [arXiv:hep-ph/0611148]

[2] C. Amsler *et al.*, *Phys. Lett.* **B667** (2008) 1

[3] I. van Vulpen, *Acta Phys. Polon.* **B38** (2007) 515

[4] A. Djouadi, *Phys. Rept.* **457** (2008) 1 [arXiv:hep-ph/0503172v2]

[5] Heavy Flavor Working Group, Private Communication.

[6] ATLAS TDR 14, CERN/LHCC 99-14

[7] ATLAS TDR 15, CERN/LHCC 99-15

[8] CERN-OPEN-2008-020

[9] M. Cacciari, M. Greco, P. Nason, *JHEP* **9805:007** [arXiv: hep-ph/9803400]

[10] P. Nason, S. Dawson, R. K. Ellis, *Nucl.Phys.* **B303** (1988) 607

[11] M. Cacciari, S. Frixione, M. L. Mangano, P. Nason, G. Ridolfi, *JHEP* **0407:033,2004** [arXiv:hep-ph/0312132v3]

[12] D. Stump *et al.* *JHEP* **0310:046,2003** [arXiv:hep-ph/0303013],
J. Pumplin *et al.* *JHEP* **0207:012,2002** [arXiv:hep-ph/0201195v3]

[13] G. P. Salam, [arXiv: 0906.1833v1]

[14] J. E. Huth *et al.*, FNAL-C-90-249-E, published in the proceedings of the 1990 Summer Study on High Energy Physics, Research Directions for the Decade, Snowmass, Colorado, June 25 July 13, 1990

[15] G. C. Blazey *et al.*, [arXiv: hep-ex/0005012v2]

[16] M. Cacciari, G. P. Salam, G. Soyez, *JHEP* **0804:063,2008** [arXiv: 0802.1189v2]

[17] ATLAS-TDR-014 ; CERN-LHCC-99-014

[18] D. López Mateos, E. W. Hughes, A. Schwartzman, ATL-COM-PHYS-2008-086

[19] S. Hassani *et al.*, *Nucl. Instr. and Meth.* **A572** (2007) 77

[20] ATL-COM-PHYS-2008-074